Nano Research

Open Access

Research Article

NiCu bifunctional electrocatalysts enable coupled anodic–cathodic nitrogen elimination with exceptional Faradaic efficiency

Chun Song, Jinjie Fang, Chengjin Chen, Yufeng Zhang, Xuejiang Zhang, Wei Zhu ✉, and Zhongbin Zhuang ✉

State Key Lab of Organic-Inorganic Composites, Beijing University of Chemical Technology, Beijing 100029, China

Cite this article: *Nano Research*, **2026**, *19*, 94908457. https://doi.org/10.26599/NR.2026.94908457

ABSTRACT: Electrochemical elimination of nitrogenous pollutants offers a sustainable solution to water eutrophication but is often limited by low efficiency when anodic and cathodic reactions are conducted separately. Herein, we report a coupled electrochemical system integrating ammonia oxidation reaction (AOR) and nitrate reduction reaction (NIRR) using bimetallic NiCu nanoalloy catalysts. Optimized Ni_5Cu_5 and Ni_2Cu_8 nanoparticles served as the anodic and cathodic catalysts, respectively, exhibiting high activity (174.7 mA·cm^{-2} @1.5 V for AOR and 84.1 mA·cm^{-2}@0 V for NIRR) and stability. A coupled full-cell electrolyzer demonstrated good stability and achieved a total nitrogen removal equivalent Faradaic efficiency of 157%. *In situ* characterizations confirmed N_2 as one of the primary products for both AOR and NIRR, along with the other nitrogenous species. These nitrogenous byproducts could be eliminated through a chemical reaction pathway, further improving the nitrogenous elimination efficiency. This work presents an efficient, noble-metal-free strategy for integrated nitrogen waste conversion, offering promising prospects for scalable wastewater treatment applications.

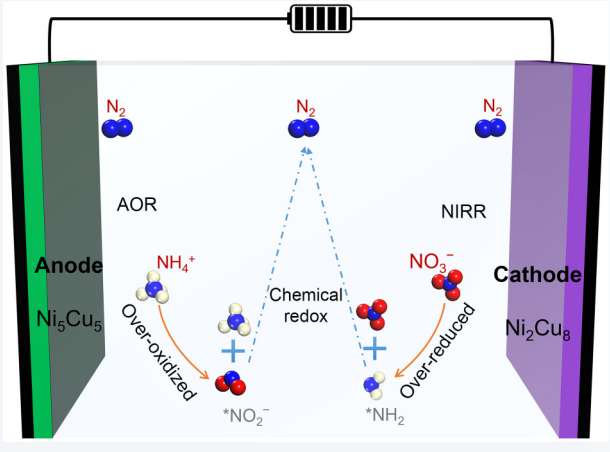

KEYWORDS: NiCu nanoalloys, coupled electrocatalysis, nitrogen elimination, bifunctional catalyst, Faradaic efficiency

1 Introduction

Inorganic nitrogen-contained wastewater, typically refers to the outlet waste containing NH_4^+, NO_3^-, or NO_2^-, is one of the primary sources that cause the eutrophication in water bodies, thus creating algal blooms and dead zones in aquatic ecosystems. Owing to the booming renewable power generation, electrochemical conversion of nitrogenous ions, including ammonia oxidation reaction (AOR) and nitrate (or nitrite) reduction reaction (NIRR), has drawn tremendous attention [1–3]. It has the advantages of mild operation condition, high efficiency, no secondary pollution, and compact facility, as compared with the classical methods (e.g., biological nutrient removal, physical-chemical process, ion exchange, etc.). With the purpose of reducing the cost of product separation and increasing the efficiency, great effort has been made to develop high-selective electrocatalysts which are essential for both the typical electrochemical conversion to N_2 and the up-to-date method to produce value-added chemicals [4–7].

However, the state-of-the-art electrocatalysts still cannot fully meet the specifications for scale application, requiring extra auxiliary processes to separate or remove the byproducts. Besides, the coupled half reaction, typically refer to hydrogen evolution reaction (HER) or oxygen evolution reaction (OER), lowers the overall reaction efficiency and the profit. Alternatively, researchers select several profitable half reactions to combine with the nitrogen-contained waste conversion half reaction, but the integrated process may be faced with more complicated separation issues [8–10]. Taking NIRR as an example, gaseous N_2 is the target product for the conventional process, and the deep reduction product of NH_3 which increases the product value is favored in the recent studies [11]. However, for both of the motivations, separation NH_3 from the electrolyte is necessary but energy-intensive. When coupling AOR with profitable half reactions (e.g., HER, CO_2 reduction reaction, etc.), the cost of the additional separation and purification processes may outweigh the added value [12–14]. Similar situations exist for the cathodic NIRR [8–10].

In view of the limited selectivity and efficiency for a separate half

Received: October 31, 2025; **Revised:** December 31, 2025
Accepted: January 17, 2026

✉Address correspondence to Wei Zhu, zhuwei@mail.buct.edu.cn; Zhongbin Zhuang, zhuangzb@mail.buct.edu.cn

reaction, combination of anodic AOR with cathodic NIRR to eliminate N-contained wastewater is a valid way to increase the efficiency and overall selectivity to gaseous N_2, avoiding the secondary pollution caused by the products of deep oxidation or reduction. The electrochemical system converts ammonium and nitrite (or nitrate) wastes into harmless N_2 simultaneously, and the over-oxidized or -reduced byproducts diffuse to the other electrodes and convert back into N_2 subsequently. The integrated system not only increase the reaction efficiency but also reduce the dependence on the selectivity of electrocatalysts. In such an oscillating system, the electrocatalysts for AOR and NIRR determines the overall Faradaic efficiency rather than the selectivity, and low cost and active electrocatalysts would be favored. For the studied noble metal-free electrocatalysts, Cu-based nanocatalysts exhibit good activity for NIRR [15–17], while Ni-based nanocatalysts are highly active to catalyze AOR [18]. The bimetallic NiCu nanocatalysts probably show higher AOR and NIRR performance than the monometallic counterparts via the alloying effect. For instance, Xu et al. have developed a hierarchical nickel-copper layered hydroxide nanowire catalyst for efficient AOR. The construction of a synergistic Ni–Cu interface through a facile hydrothermal synthesis followed by electrochemical activation significantly enhanced the AOR of nickel‑based catalysts [19]. Wang et al. have prepared copper‑nickel alloy catalysts for NIRR to ammonia, demonstrating that alloying Cu with Ni tunes the electronic structure and enhances catalytic performance. The improved activity and selectivity are attributed to an upshifted d-band center that optimizes the adsorption energies of key intermediates and lowers the reaction overpotential [20]. Hence, integrating these distinct yet synergistic catalytic functions into a unified electrochemical system, where bifunctional NiCu catalysts serve simultaneously as anode and cathode to convert ammonium and nitrate/nitrite contaminants into harmless N_2, represents an efficient strategy for complete nitrogen removal-leveraging the complementary activities of Ni and Cu while overcoming the selectivity limitations of standalone half-reactions.

Herein, we presented an AOR-NIRR-coupled electrochemical nitrogen-contained waste eliminator using NiCu bimetallic NPs electrocatalysts as the anodic and cathodic electrocatalysts. The composition of the bimetallic catalysts was optimized for AOR and NIRR separately. The electrocatalytic activity of the optimal electrocatalysts surpassed the other counterparts, suggesting the probable alloying and composition effects. N_2 was determined to be the main product with non-negligible by-products. By assembling the full-cell electrolyzer using the NiCu NPs, relatively high stability and superior total nitrogen removal equivalent Faradaic efficiency were achieved. Possible electrochemical-triggered redox reaction mechanism was proposed.

2 Experimental section

2.1 Chemical

All chemicals were of reagent grade and used without further purification: nickel(II) acetylacetonate ($Ni(acac)_2$, 99%, aladdin), cupric(II) acetylacetonate ($Cu(acac)_2$, 99.9%, aladdin), oleylamine (90%, aladdin), ethanol (> 99.5%, Sinopharm), KNO_3 (99.9%, aladdin), ammonia (99.999%, Alfa), cyclohexane (> 99.5%, Sinopharm), potassium hydroxide (99.999%, Alfa), sodium hydroxide (99.999%, Alfa), sulfuric acid (98%, Sinopharm), hydrochloric acid (37%, Tongguang), sodium nitroprusside (90%, Macklin), sodium citrate (> 99%,Macklin), nafion solution (5%, Dupont), salicylic acid (> 99%, aladdin), and sodium hypochlorite (0.5 $mol \cdot L^{-1}$, Tanmo).

2.2 Synthesis of NiCu/C bimetallic catalysts

In the typical synthesis of NiCu bimetallic catalysts, $Ni(acac)_2$ and $Cu(acac)_2$ with different Ni:Cu molar ratios (i.e., 0:10, 2:8, 5:5, 8:2, and 10:0) were dissolved into 15 mL of oleylamine and transferred into a 40 mL Teflon-lined autoclave. The total molar quantity of the metal precursors was 1.0 mmol. Then, the sealed autoclave was heated to 180 °C and kept for 15 h. After cooling down to room temperature, the product was precipitated by adding ethanol and separated using centrifugation. The product was washed by the mixture of ethanol and cyclohexane several times and finally dispersed in cyclohexane. The Vulcan 72X carbon powder was pretreated at 500 °C in the air atmosphere for 5 h. The cyclohexane solution containing NiCu were mixed with 50 mg of the pretreated carbon powder and stirred overnight. Finally, the NiCu/C product was separated by filtration and dried at 50 °C overnight.

2.3 Characterizations

The catalysts were thoroughly analyzed for their chemical composition and microstructure using various analytical techniques. Transmission electron microscopy (TEM, FEI Talos F200x) and high-resolution TEM (HRTEM, JEOL JEM-2010F) were employed to examine the microstructure in detail. The crystalline phase was characterized by X-ray diffraction (XRD, Rigaku D/Max 2500 VB2+/PC) with a scanning rate of 5 $°\cdot min^{-1}$ and a 2θ range from 10° to 90°. X-ray photoelectron spectroscopy (XPS, Thermo Scientific K-Alpha) with an Al Kα excitation source ($h\nu$ = 1486.8 eV) was utilized to determine the chemical states of the catalysts. The metal content was monitored by inductively coupled plasma-optical emission spectroscopy (ICP-OES), which was carried out on Thermo Fisher IRIS Intrepid.

2.4 Electrochemical tests

Electrochemical measurements were performed using an electrochemical workstation (Princeton Applied Research, V3) with a standard three-electrode system at room temperature. The reference electrode is a mercury/mercury oxide (Hg/HgO) electrode and the counter electrode was a carbon rod. The catalyst ink was prepared by dispersing 1 mg of catalyst powder in 1 mL of a mixed solution containing ethanol (800 μL), water (190 μL), and Nafion (5 wt.%, 10 μL). A 40 μL aliquot of the catalyst ink was deposited onto a glassy carbon electrode (5 mm in diameter, PINE instruments) in five separate 8 μL increments, to serve as the working electrode. Deionized water (18.2 MΩ·cm) was used in all electrochemical experiments. All potentials reported in this study were converted to the reversible hydrogen electrode (RHE) scale. The solution resistances, measured via AC impedance spectroscopy, were corrected for in the polarization curves.

2.5 AOR-NIRR-coupled electrolyzer measurements

The electrolyte prepared for the selective determination was performed using the same electrochemical workstation but in a single chamber using a two-electrode and membrane-free system. Both the working electrode and the counter electrode were carbon papers (28BC, Sigracet, SGL Carbon) coated with catalysts powder.

The catalyst ink preparation method is the same as described above, with the only modification being the concentration adjusted to 2 mg·mL^{-1}. The catalyst ink was drop-coated onto one side of the carbon paper, covering an area of 1 cm^2, with a coating amount of 1 mg. The initial electrolyte consists of 1 M KOH, 0.1 M ammonia, and 0.1 M potassium nitrate. The constant potential test was directly conducted based on the CV curves without IR compensation. AOR takes place at the anode, while NIRR take place at the cathode.

2.6 Selectivity determination

The concentration of ions involved in the experiment was measured using ion chromatography (Thermo Fisher Scientific Dionex Aquion), equipped with an electrical conductivity detector (DS6 HEATED CONDUCTIVITY CELL), suppressor (CSRS300), autosampler, protective column, and analytical columns (CG12 (2 × 50 mm) and CS12 (4 × 250 mm)). The eluent used was a 20 mM methylsulfonic acid solution, with a flow rate of 1 mL·min^{-1}. The suppressor current was set at 71 mA, and the column temperature was maintained at 30 °C. The retention times for anions and cations were 4.59 min and 5.28 min, respectively.

2.7 *In situ* experiments

The electrochemical *in situ* attenuated total reflection-surface enhanced infrared absorption spectroscopy (ATR-SEIRAS) spectra were taken with a Nicolet iS50 Fourier transform-infrared (FT-IR) spectrometer equipped with an MCT detector cooled with liquid nitrogen and a PIKE VeeMAX III variable angle ATR sampling accessory. The spectral resolution was set to 4 cm^{-1} and 64 interferograms were coadded for each spectrum. The spectra are given in absorption units defined as $A = -\lg(R/R_0)$, where R and R_0 represent the reflected intensities corresponding to the sample and reference-single beam spectrum, respectively. A 60° Si face-angled crystal was used as the reflection element. The angle of incidence was set as ca. 70°. The ultrathin Au film was deposited chemically in it for IR-signal enhancement and conduction of electrons. The electrocatalyst was dropped onto the Au film to serve as a working electrode for SEIRAS experiments with a loading of 0.05 mg·cm^{-2}. The catalysts fully covered the Au film. A platinum wire and an Ag/AgCl electrode were used as the counter and reference electrode in all tests, respectively. The chronopotentiometry method was used in this experiment at different potentials (−0.25 to 0.35 V vs. RHE for NIRR and 1.25 to 1.75 V vs. RHE for AOR both without iR correction). The SEIRAS spectra were collected during the chronopotentiometry test. The reference-single beam spectrums are collected at −0.25 and 1.25 V.

Differential electrochemical mass spectrometry (DEMS) was performed using a QAS 100 DEMS system provided by Linglu Instruments (Shanghai) Co. Ltd. Electrochemical online DEMS measurements were conducted using a mass spectrometer coupled with an electrochemical workstation. The electrolytes were 1 M KOH with 0.1 M NH_3 and 1 M KOH with 0.1 M KNO_3. The working electrode was a carbon substrate coated with the as-prepared sample, while a Pt wire and an Ag/AgCl electrode served as the counter and reference electrodes, respectively. Throughout the experiment, argon gas was continuously purged into the electrolyte to maintain an inert atmosphere. A potentiostatic test was performed at 1.235 and 0.335 V, respectively, with simultaneous acquisition of the corresponding mass signals. Data from there measurement cycles were collected for analysis.

3 Results and discussion

A series of NiCu bimetallic NPs with different Cu:Ni ratios (i.e., 10:0, 8:2, 5:5, 2:8, and 0:10 in atomic ratio) were synthesized using a typical wet-chemistry method. In the synthesis, Ni(acac)$_2$ and Cu(acac)$_2$ were used as the metal precursors, and oleylamine served as the capping agent and reductant. As shown in Figs. 1(a) and 1(b) and Figs. S1(a)–S1(c) in the Electronic Supplementary Material (ESM), the NiCu samples were the mixture of spherical and branched particles with several hundred nanometers in size. Figure 2(a) and Fig. S2 in the ESM show the XRD patterns of the NiCu particles. The peaks of the Ni_2Cu_8 particles fell between those of Ni (JCPDS No. 04-0850) and Cu (JCPDS No. 85-1326), suggesting the formation of alloy with fcc structure according to the Vegard's law. However, there were two sets of fcc-structured diffraction peaks for the Ni_5Cu_5 and Ni_8Cu_2. For the Ni_5Cu_5 NPs, the more intensive diffraction peak group could be assigned to the NiCu alloy while the less intensive peak set at higher diffraction angle could be segregated Ni. Similarly, NiCu alloy and segregated Ni were also observed in the Ni_8Cu_2 sample, suggesting that Ni was prone to segregate in the Ni-enriched NiCu bimetallic NPs. As shown in Table S1 in the ESM, the ICP-OES tests demonstrated the Cu:Ni ratios were close to the precursor ratios, suggesting that almost all the precursors were reduced to form the NPs. Then, the Ni_2Cu_8 and Ni_5Cu_5 NPs were selected as the representative to examine the microstructure using high-resolution TEM (HRTEM) equipped with an energy dispersive X-ray spectrometer (EDS). As shown Figs. 1(c) and 1(d), the HRTEM image indicated the polycrystalline structure of the NiCu NPs with abundant grain boundaries. The lattice fringes suggested the typical fcc structure, consistent with the XRD results. The HAADF-STEM EDS mapping profiles, i.e., Figs. 1(e) and 1(f), suggested the partial segregation of Ni surrounding the NiCu particles, in line with the XRD results. The segregation was more significant for the Ni_5Cu_5 than the Ni_2Cu_8 from the mapping profiles, also consistent with the negligible XRD peaks of segregated Ni for the Ni_2Cu_8. Moreover, the large particles were usually Cu-enriched, and the surroundings were the segregated Ni NPs. It might result from the metallicity difference of the two metals, and thus Cu was reduced prior to Ni.

XPS analysis was conducted on the samples to determine the surface chemical status of the NiCu NPs. Figures 2(b)–2(d) show the high-resolution Ni 2p, Cu 2p, and Cu LMM Auger spectra respectively. For the Ni 2p spectra, the peak at 852.9 eV was assigned to Ni(0), and the peak at 855.6 eV was assigned to Ni(II) with an intensive satellite peak from 858 to 868 eV [21]. For the Cu 2p spectra, the peak at 935.0 eV was assigned to Cu(II), along with an intensive shake-up line from 938 to 948 eV, while the peak at 932.8 eV could be assigned to either Cu(0) or Cu(I) [22]. The peak fitting results suggested the existence oxidized Ni and Cu at the surface of the samples. The Ni 2p XPS spectra suggested that the co-existence of NiO and Ni(OH)$_2$ on the surface of Ni_5Cu_5 and the surface species on the Ni_2Cu_8 NPs were mainly Ni(OH)$_2$. The Cu LMM Auger spectrum peak of the Ni_2Cu_8 centered at 915.9 eV suggested the presence of Cu_2O species on the surface. These oxidized peaks might be attributed to the surface oxidation of samples when exposing in the air. Synchrotron-based X-ray adsorption near edge structure (XANES) spectroscopy was conducted on the samples as shown in Fig. S3 in the ESM. Both the near edge spectra of the NiCu samples were close to the metal foils, suggesting the metallic state of the samples in bulk. Nevertheless, the Ni K edge near edge spectra of the NiCu bimetallic samples

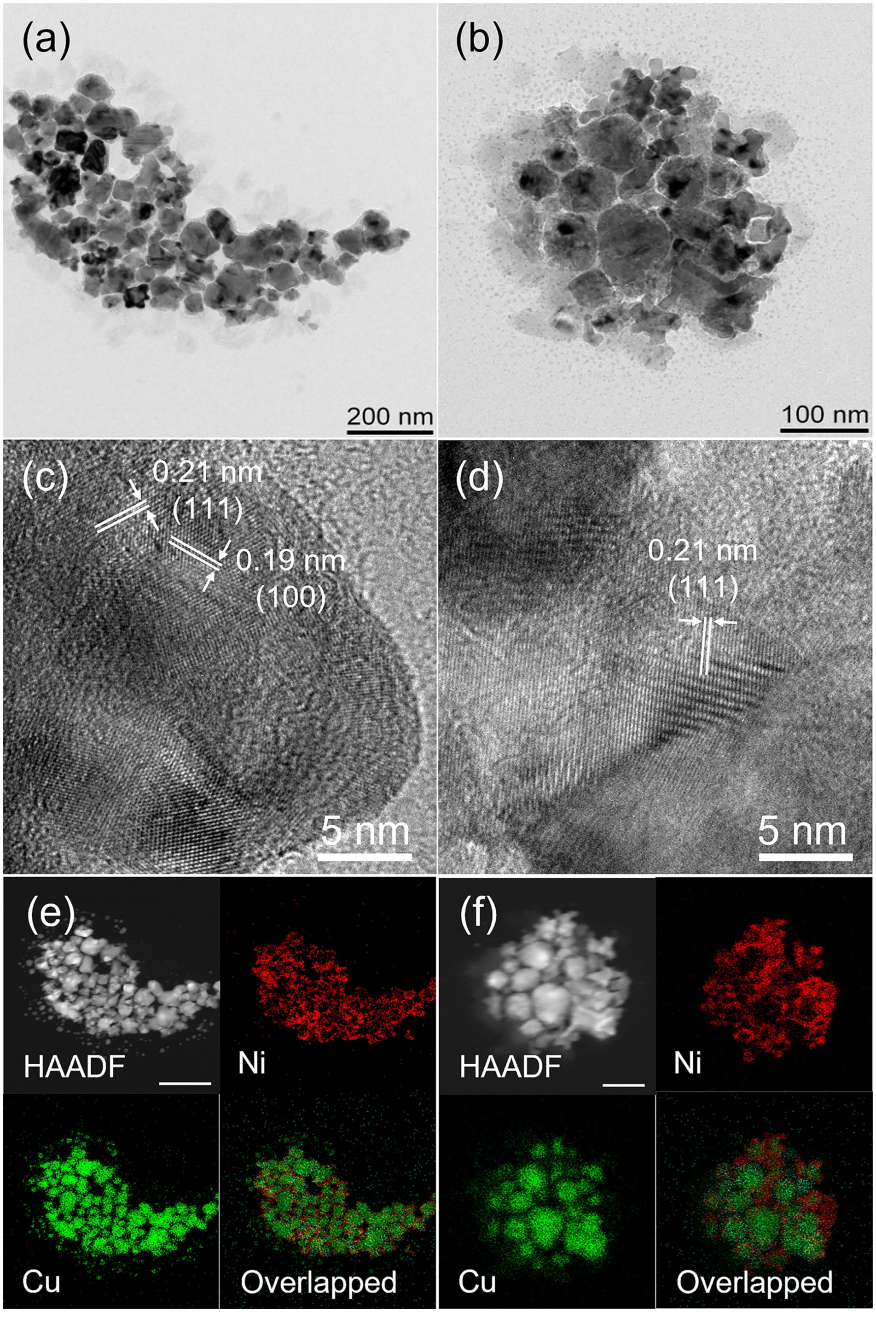

Figure 1 (a) TEM image, (c) HRTEM image, and (e) HAADF-STEM EDS mapping profiles of the Ni_2Cu_8 catalyst. (b) TEM image, (d) HRTEM image, and (f) HAADF-STEM EDS mapping profiles of the Ni_5Cu_5 catalyst.

shifted to the high energy slightly as compared with the Ni foil, while the Cu K edge near edge spectra of the bimetallic samples shifted to the low energy slightly as compared with the Cu foil as well. It suggested the probable charge transfer from Ni to Cu and the metallic state for the NiCu samples, which was consistent with the aforementioned characterizations.

A typical three-electrode system was used to evaluate the electrocatalytic performance of the NiCu bimetallic catalysts for the anodic AOR and the cathodic NIRR. A linear scanning voltammetry (LSV) method was performed to obtain the polarization curves for AOR and NIRR as shown in Figs. 3(a)–3(d). As illustrated in Figs. 3(a) and 3(b), 1.0 M KOH electrolyte with and without the reactants were used to tell AOR and NIRR from oxygen evolution reaction (OER) and hydrogen evolution reaction (HER) respectively. It was suggested that no significant OER took place for the Ni_5Cu_5 below 1.54 V while no HER took place for the Ni_2Cu_8 above −0.20 V. With the introduction of NH_4^+ in the electrolyte, the anodic current density significantly increases, indicating the ability of conduct the AOR (Fig. 3(a)). With the introduction of NO_3^- in the electrolyte, the cathodic current density significantly increases, indicating the ability of conduct the NIRR (Fig. 3(b)).

Figure 3(c) shows the polarization curves of the series of NiCu bimetallic catalysts for AOR, demonstrating that the Ni_5Cu_5 NPs exhibited the highest catalytic activity. The onset potential of the Ni_5Cu_5 NPs for AOR was 1.3 V (vs. RHE, the same hereafter),

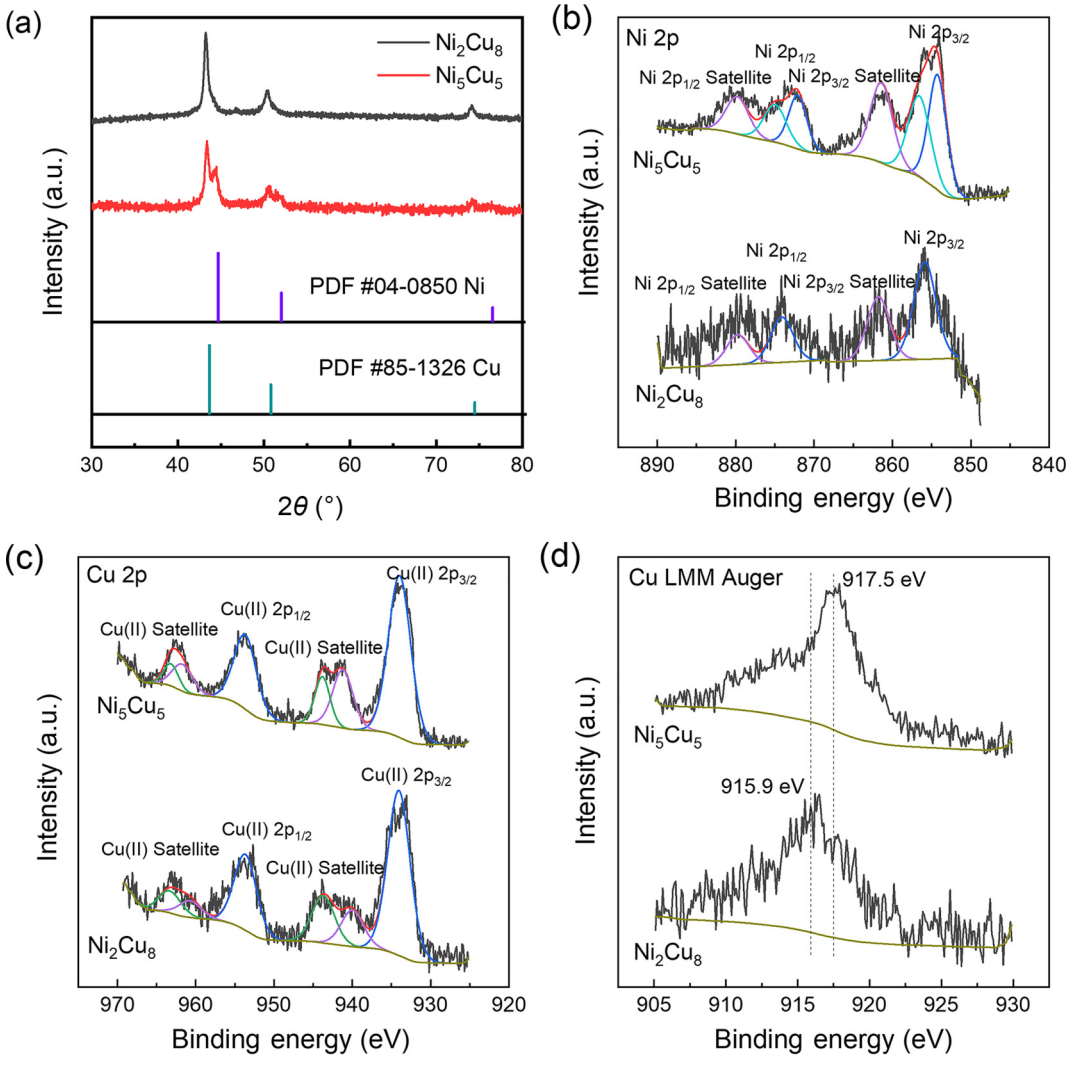

Figure 2 (a) XRD patterns, (b) Ni 2p XPS, (c) Cu 2p XPS, and (d) Cu LMM Auger spectra of the Ni_2Cu_8 and Ni_5Cu_5 catalysts.

much lower than those of the other NiCu NPs. The current density reached the peak value at about 1.6 V, where OER just started for the Ni_5Cu_5 NPs as evidenced from the test in the electrolyte without ammonia, suggesting that the anodic current was primarily contributed from AOR rather than OER. It was also indicated that OER possibly impeded AOR at the high potential region, leading to the formation of oxidation peak for AOR. The AOR performance of the monometallic NPs suggested that both Cu and Ni NPs showed comparable AOR activity except that Cu was the better one at the potential interval from 1.5 to 1.7 V. The current density at 1.5 V were used as the criterion to quantify the AOR activity. As shown in Fig. 3(e), the Ni_5Cu_5 NPs showed the highest current density of 174.7 mA·cm^{-2}, 26 times higher than the second-best catalyst (Ni_8Cu_2 NP, 6.6 mA·cm^{-2}). For the cathodic NIRR, as illustrated in Fig. 3(d), the Ni_2Cu_8 NP exhibited the highest cathodic current density and the highest onset potential (ca. 0.2 V) amongst all the tested samples. The test performed on the electrolyte without NO_3^- demonstrated that the Ni_2Cu_8 NP showed little HER activity above −0.20 V (Fig. 3(b)), suggesting that the cathodic current density was mainly contributed from NIRR. The monometallic NP also showed NIRR activity below 0.10 V, and the activity of the Cu NP surpassed those of the Ni NP and the other NiCu NPs, indicating that Cu was the main active site and only an appropriate Ni:Cu ratio would enhance the NIRR activity of Cu. Using the cathodic current density at 0 V as the criterion of NIRR activity, the Ni_2Cu_8 NP exhibited a cathodic current density of 84.1 mA·cm^{-2}, 2.6 times higher than the second-best catalyst (Cu, 31.6 mA·cm^{-2}) as shown in Fig. 3(e). Similarly, an appropriate Ni:Cu ratio was equally important for the cathodic NIRR catalysts. Based on the previous report by Wang et al, the probable ligand effect via the charge transfer between Ni and Cu that was evidenced by the XANES optimized the adsorption energies of the intermediates (*NO_3^-, *NO_2, *NH_2) for both NIRR and AOR, and thus enhanced the electrocatalytic activity.

As illustrated in Fig. 4(a), the proposed electrolyzer using Ni_5Cu_5 NPs as the anodic catalyst and Ni_2Cu_8 NPs as the cathodic catalyst was assembled to eliminate the nitrogenous contaminants in the solution. An electrolyte containing 0.1 M NH_4^+ and 0.1 M NO_3^- was used as the representative pollutant, and the stability and Faradaic efficiency were evaluated using the electrolyzer. Monometallic Ni and Cu were also adopted as the references in the device study. The electrolyzer already worked from the initial 1.0 V, and the current density increased with the increase of the applied voltage within 1.7 V. Chronoamperometry at 1.5 V was used to evaluate the stability as illustrated in Fig. 4(b). The electrolyzer retained 34% of the initial current density (22.6 mA·cm^{-2}) after the 5 h' operation.

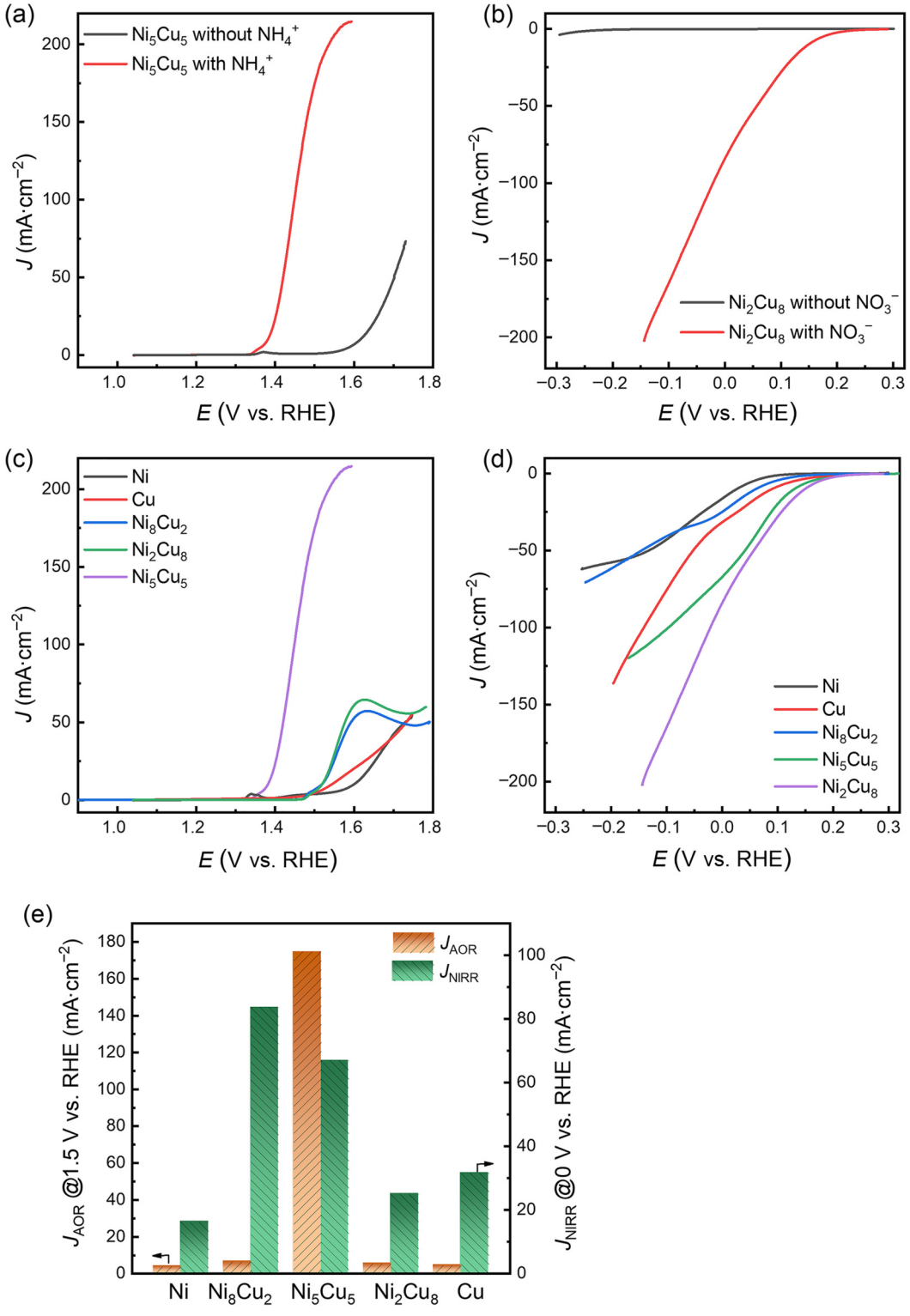

Figure 3 Polarization curves of the NiCu catalysts in the solution with and without (a) NH_4^+ and (b) NO_3^-. Polarization curves of the NiCu catalysts and references for (c) AOR and (d) NIRR. (e) The activity comparison of the samples for AOR and NIRR.

However, the monometallic NPs deactivated quickly in the stability tests as shown in Fig. 4(b), suggesting the high stability of the electrolyzer using the NiCu catalysts.

XPS characterizations were conducted on the cathodic Ni_2Cu_8 and anodic Ni_5Cu_5 samples to reveal the probable evolution of surface chemistry during the reactions. Figure S4 in the ESM shows the Ni 2p, Cu 2p, and Cu LMM Auger XPS spectra of both the catalysts before and after the samples. For the cathodic Ni_2Cu_8 catalyst, the Ni $2p_{3/2}$ peak centered at 856.0 eV didn't shift during the NIRR, suggesting that Ni was mainly in the form of $Ni(OH)_2$. According to the Cu 2p and LMM Auger spectra in Figs. S4(b) and S4(c) in the ESM, Cu was mainly in the form of oxides during the

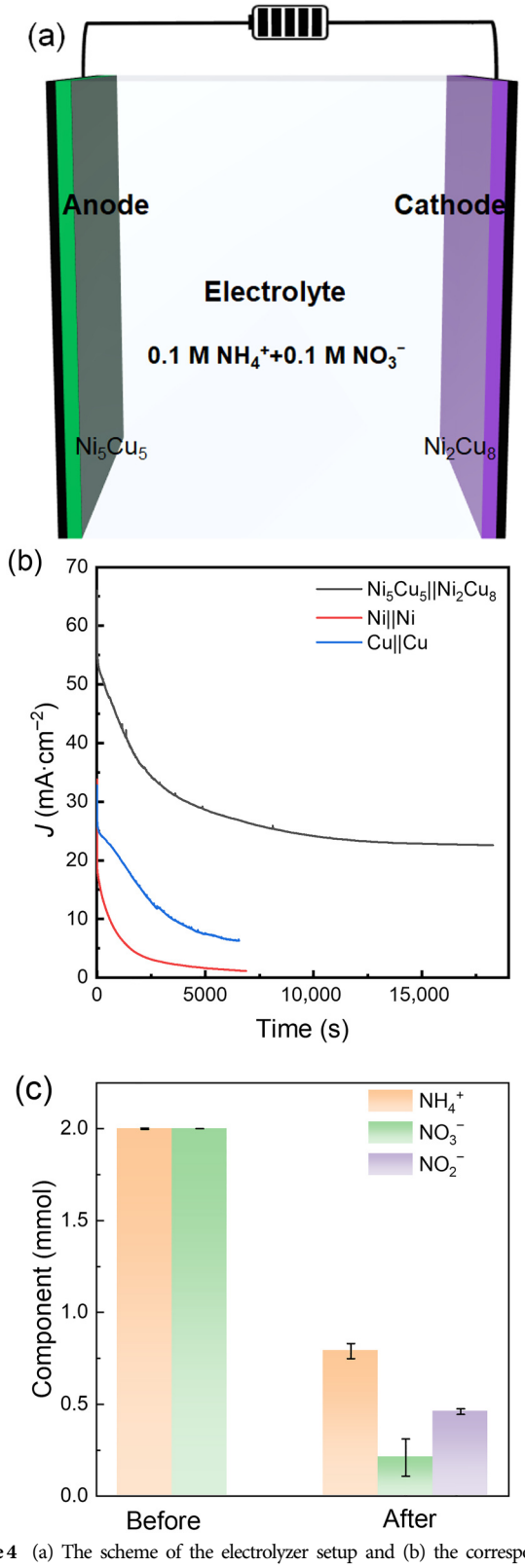

Figure 4 (a) The scheme of the electrolyzer setup and (b) the corresponding chronoamperometric test at 1.5 V in in a 20 mL of electrolyte containing 0.1 M NH_4^+ and 0.1 M NO_3^-. (c) The composition of nitrogenous species in the electrolyte before and after the electrolysis.

reaction. For the Ni_2Cu_8 catalyst, the surface chemical state didn't change significantly during the NIRR, but the Ni:Cu ratio decreased from 0.57 to 0.16, suggesting the more preferential dissolution of Ni than the Cu during NIRR. For the anodic Ni_5Cu_5 catalyst, as shown in Fig. S4(d) in the ESM, the fitting peak of the Ni $2p_{3/2}$ spectra at 854 eV decreased with the increase of the fitting peak at 856 eV, suggesting the formation of high-valence Ni species during the anodic AOR. However, for the Cu 2p spectra, an intensive fitting peak at 932.6 eV generated during the AOR, which could be assigned to either Cu_2O or Cu. As shown in Fig. S4(f) in the ESM, the Cu LMM Auger peak shifted to the low kinetic energy, suggesting the formation of Cu_2O on the surface. Moreover, the Ni:Cu ratio increased from 1.3 to 2.0, suggesting the preferential dissolution of Cu during AOR. It was deduced that the coordination dissolution of Cu(II) in the ammonia-contained solution was the probable origin for the surface evolution of the Ni_5Cu_5 catalyst. The dissolution of catalyst could also be responsible for the degradation of catalytic performance.

The change of nitrogenous ion concentrations (i.e., NH_4^+, NO_2^-, NO_3^-) in the stability tests were monitored using the ion chromatography, and the Faradaic efficiency was calculated [23]. After the 5 h' operation, 1.21 mmol of NH_4^+ and 1.79 mmol of NO_3^- were converted, along with the formation of 0.46 mmol of NO_2^- (Fig. 4(c)). Assuming that the lost nitrogen-containing species in the solution were all converted to nitrogen gas, the indirect nitrogen gas production was estimated to be 1.27 mmol. Because the consumption of NO_3^- was much higher than that of NH_4^+, we assumed that all the generated NO_2^- was converted from NIRR and all the ammonium ion converted into N_2 through AOR to estimate the minimum apparent Faradaic efficiency. The apparent Faradaic efficiency for AOR (F.E.-AOR) was estimated by eliminated NH_4^+ using Eq. (1).

$$\text{F.E.-AOR} = \frac{3n\left(\text{NH}_4^+\right)_{\text{converted}} F}{\int_0^t I_t \mathrm{d}t} \quad (1)$$

where F is the Faraday's constant (96,485 C·mol^{-1}), It is the current at time t, and t is the elapsed time. The estimated F.E.-AOR was 75%, suggesting that probable side reactions took place at the anode. Due to the low OER activity of the Ni_5Cu_5 NPs, it is possible that NH_4^+ is generated from the cathodic NIRR to lower the F.E.-AOR. Due to NIRR occurs on the cathode, it also contributed to the elimination of nitrogenous compound, the total nitrogen removal equivalent Faradaic efficiency for elimination of nitrogenous compound (i.e., N_2 generation) (denoted as F.E.-total) was estimated using Eq. (2).

$$\text{F.E.-total} = \frac{6n\left(\text{N}_2\right)_{\text{generated}} F}{\int_0^t I_t \mathrm{d}t} \quad (2)$$

The F.E.-total is 157%, due to the nitrogen removal exists in both anode and cathode. It demonstrates the advantage of the AOR and NIRR coupled electrolyzer design.

It should be noted that an unexpected high apparent Faradaic efficiency is achieved from the cathode side. Given that all the NO_2^- generated from cathode side and apparent Faradaic efficiency for NIRR (F.E.-NIRR) was estimated by eliminated NO_3^- using Eq. (3).

$$\text{F.E.-NIRR} = \frac{5\left(n\left(\text{NO}_3^-\right)_{\text{converted}} - n\left(\text{NO}_2^-\right)_{\text{generated}}\right) F}{\int_0^t I_t \mathrm{d}t} \quad (3)$$

Unexpectedly, the estimated apparent F.E.-NIRR for the cathodic NIRR was 137%, far exceeding the theoretical value of 100%. It was deduced that the elimination reaction was not completely driven by

the electrochemical process. Chemical process also coupled with in the device. Table S2 in the ESM also summarizes the device performance of the similar coupled systems [3, 24–29]. As compared with the reported systems, this AOR-NIRR coupled system had the advantages of relative-low energy consumption, exceptional-high total nitrogen removal equivalent Faradaic efficiency, and no further separation requirements.

To figure out the probable mechanism for the unexpected high total nitrogen removal equivalent Faradaic efficiency, we conducted *in situ* electrochemical ATR-SEIRAS and DEMS to determine the intermediates and products for AOR and NIRR [30–34]. As shown in Figs. 5(a) and 5(b), the broad band at 3200–3400 cm^{-1} and the band at ca. 1650 cm^{-1} were assigned to the adsorbed interfacial H_2O, suggesting that interfacial water participated in both the AOR and NIRR since the band intensities increased with the increment of overpotentials. The formation potentials of the interfacial water from the ATR-SEIRAS spectra were almost the same as the onset potentials for both AOR and NIRR, demonstrating the key role of the interfacial water in the electrocatalysis. For the NiCu-catalyzed AOR in Fig. 5(a), the absorption bands at the difference spectra were almost positive-going, suggesting that the bands were related to the intermediates or the products. Because the absorption band of NH_3 at ca. 1600 cm^{-1} might overlap with that of H_2O at ca. 1650 cm^{-1}, the consumption of NH_3 could not be observed from the spectra. The bands at 1450, 1340, and 1234 cm^{-1} assigned to the vibration of NO_2^- and NO_3^- increased, suggested adsorbed NO_2^- and NO_3^- on the CuNi catalyst surface for AOR. As gaseous NO is the decomposition product of NO_2^-, the signals of N_2 and NO in the DEMS (Figs. 5(c) and 5(d)) also confirmed that the deep-oxidation reaction to NO_2^- or NO_3^- also took place for the CuNi-catalyzed AOR. The apparent Faradaic efficiency of AOR could be higher than the estimated minimum value, and the same applies to the cathodic NIRR. For the NiCu-catalyzed NIRR in Fig. 5(b), the negative-going bands at 1440, 1344, and 1210 cm^{-1} were probably due to the consumption of nitrate and nitrite with the overpotential increment. The negative-going band of nitrite suggested that the already happened conversion from nitrate to nitrite at the potential of the reference spectrum. Similarly, the absorption band of ammonia product at ca. 1600 cm^{-1} also overlapped with the band of water. As shown in Figs. 5(e) and 5(f), NH_3, N_2, and H_2 were detected for CuNi-catalyzed NIRR using DEMS, suggesting that and ammonia was probably the main product of NIRR along with HER and NIRR to N_2.

Hence, the *in situ* characterizations demonstrated that both AOR and NIRR catalyzed by NiCu alloys showed certain selectivity to N_2 along with side reactions, and several kinds of nitrogenous intermediates generated. The cathode reduction product could be further oxidized at anode, and vice versa. For example, NH_3 generated at the cathode, and it was further oxidized at anode. This process lowers the total nitrogen removal equivalent Faradaic efficiency for the electrochemical process. However, chemical process may occur after the electron transfer steps on the electrode within the nitrogenous intermediates, and thus N_2 produces via a non-electrode process. For example, $*NH_2$ and $*NO_2^-$ were observed by the *in situ* FTIR. Because nitrite has stronger oxidizing capacity and reactivity compared to nitrate, it is more likely to react as an intermediate with reducing intermediates such as ammonia species, producing substances like nitrogen gas. It has been reported that Cu catalyze the combination of NO_2^- with NH_3 to form N_2 through the reaction of $*NO_2^- + NH_3 \rightarrow N_2 + H_2O + OH^- + *$, and thus provide an addition non-electrochemical reaction pathway to eliminate nitrogenous species [35]. As schemed in Fig. 5(g), these nitrogenous species eliminated from non-Faradaic process triggered extra chemical elimination pathway, resulting in the exceptional apparent Faradaic efficiency [36].

Compared to the other systems coupling AOR or NIRR with HER or OER, which often face challenges in product separation and value recovery, our nitrogen-focused coupling strategy offers a more direct route for total nitrogen removal without the need for energy-intensive downstream separation. While recent studies focus on the valuable NH_3 production from NIRR, our approach is particularly suited for wastewater treatment where complete detoxification to N_2 is the primary goal. The stability retained over 5 h and the use of non-precious NiCu catalysts further enhance the practical appeal. Although tested in a simulated electrolyte, the system's operation in a mixed, concentrated nitrogenous environment suggests potential robustness. A preliminary estimate based on our operating voltage (1.5 V) and current indicates promising energy efficiency for nitrogen removal, which could be competitive upon scaling and optimization. However, challenges remain for practical deployment, including the need to further enhance current density for faster treatment, understand long-term stability under variable wastewater matrices, and potentially manage NO_2^- accumulation in some scenarios. Nonetheless, this study establishes a proof-of-concept for an efficient, noble-metal-free, and coupled electrochemical strategy that transforms the challenge of nitrogenous pollutant elimination into a synergistic process with high Faradaic efficiency.

4 Conclusion

In sum, we adopted NiCu bimetallic NP electrocatalysts for both AOR and NIRR to eliminate nitrogenous wastes with high overall efficiency. By varying the Ni:Cu ratios, optimal NiCu electrocatalysts for AOR and NIRR were screened separately, surpassing the monometallic counterparts and the NiCu NPs with the other compositions. A full-cell electrolyzer was assembled by integrating anodic AOR and cathodic NIRR using NiCu electrocatalysts. The quantitative analysis results of solution demonstrated high total nitrogen removal equivalent Faradaic efficiency of 157%, displaying the advantages of the coupled anodic-cathodic nitrogen elimination electrochemical cell design. *In situ* electrochemical characterizations revealed that N_2 was the main product for both AOR and NIRR along with non-negligible side reactions. The nitrogenous byproduct could be eliminated through a chemical elimination reaction, achieving the superior elimination efficiency. This study provides an efficient method to remove nitrogenous wastes using non-precious metal electrocatalysts.

Electronic Supplementary Material: Supplementary material (TEM, XRD, XANES, XPS, ICP-OES, and device performances reported in the literature) is available in the online version of this article at https://doi.org/10.26599/NR.2026.94908457.

Data availability

All data needed to support the conclusions in the paper are presented in the manuscript and the Electronic Supplementary Material. Additional data related to this paper may be requested from the corresponding author upon request.

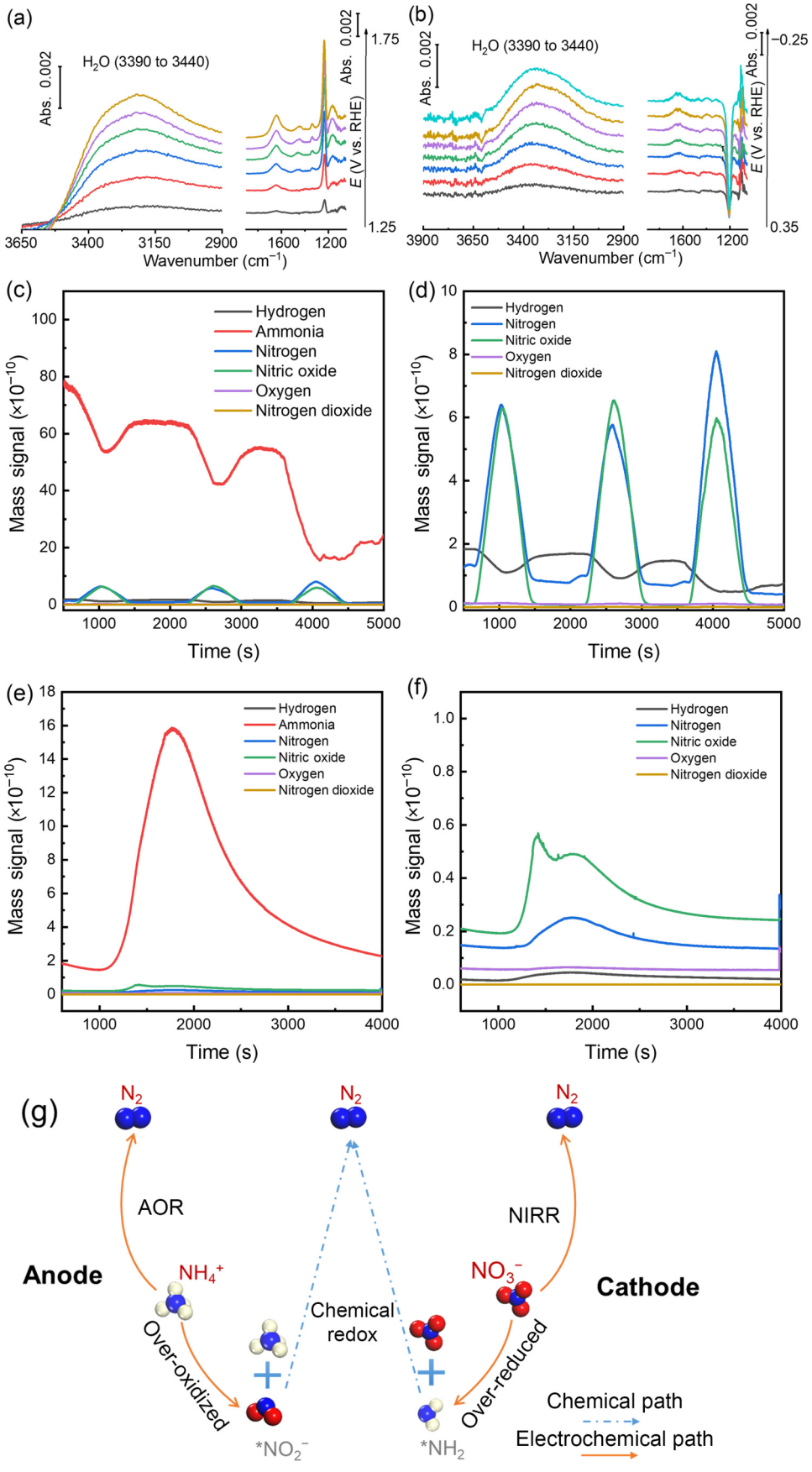

Figure 5 *In situ* electrochemical ATR-SEIRAS spectra of (a) Ni_5Cu_5-catalyzed AOR and (b) Ni_2Cu_8-catalyzed NIRR. *In situ* electrochemical DEMS of ((c) and (d)) Ni_5Cu_5-catalyzed AOR and ((e) and (f)) Ni_2Cu_8-catalyzed NIRR, and the latters are the magnified spectra of the formers. (g) The reaction mechanism of the electrolyzer.

Acknowledgements

The authors acknowledge the financial support by the Energy Revolution S&T Program of Yulin Innovation Institute of Clean Energy (No. YIICE E411090316) and the National Natural Science Foundation of China (Nos. 22279004 and 22379004). The authors appreciate the BL14W1 in the Shanghai Synchrotron Radiation Facility (SSRF) for help with XAFS experiments. This paper is in memory of Prof. Xin Liang.

Declaration of competing interest

All the contributing authors report no conflict of interests in this work.

Author contribution statement

C. S.: Data curation, validation, writing manuscript, experimental design. J. J. F.: Data curation, validation. C. J. C.: Data curation, validation. Y. F. Z.: Validation. X. J. Z.: Validation. W. Z.: Writing manuscript, experimental design. Z. B. Z.: Project administration, funding acquisition, writing manuscript. All the authors have approved the final manuscript.

Use of AI statement

None.

References

[1] Sun, M. L.; Wang, H. Y.; Feng, Y.; Ren, J. T.; Wang, L.; Yuan, Z. Y. Electrodegradation of nitrogenous pollutants in sewage: From reaction fundamentals to energy valorization applications. *Chem. Soc. Rev.* **2024**, *53*, 11908–11966.

[2] Zhang, K. E.; Zou, X. H.; Liu, Y.; Zhang, X.; An, L. Progress and perspectives in the electroreduction of low-concentration nitrate for wastewater management. *iScience* **2025**, *28*, 111687.

[3] Wang, Y. J.; Yu, W. Q.; Li, X.; Yu, J. Y.; Zhou, W. J. Electrocatalytic reduction of nitrogenous pollutants to ammonia. *Chem. Eng. J.* **2023**, *469*, 143889.

[4] Wu, Q. L.; Zhu, F. F.; Wallace, G.; Yao, X. D.; Chen, J. Electrocatalysis of nitrogen pollution: Transforming nitrogen waste into high-value chemicals. *Chem. Soc. Rev.* **2024**, *53*, 557–565.

[5] Liu, J. W.; Li, Z. Y.; Lv, C. D.; Tan, X. Y.; Lee, C.; Loh, X. J.; Chua, M. H.; Li, Z. B.; Pan, H. G.; Chen, J. et al. Electrocatalytic upgrading of nitrogenous wastes into value-added chemicals: A review. *Mater. Today* **2024**, *73*, 208–259.

[6] Yi, M.; Li, H. M.; Xie, M. H.; Li, P. P.; Jin, Z. Y.; Yu, G. H. Electrocatalysis for sustainable nitrogen management: Materials innovation for sensing, removal and upcycling technologies. *Sci. China Chem.* **2025**, *68*, 2322–2342.

[7] Wang, D. D.; Lu, X. F.; Luan, D. Y.; Lou, X. W. Selective electrocatalytic conversion of nitric oxide to high value-added chemicals. *Adv. Mater.* **2024**, *36*, 2312645.

[8] Li, J. Z.; Li, H.; Fan, K.; Lee, J. Y.; Xie, W. F.; Shao, M. F. Electrocatalytic nitrate reduction to ammonia coupled with organic oxidation. *Chem Catal.* **2023**, *3*, 100638.

[9] Lu, Y. X.; Yue, F.; Liu, T. Y.; Huang, Y. C.; Fu, F.; Jing, Y.; Yang, H. Q.; Yang, C. M. Size-effect induced controllable Cu^0-Cu^+ sites for ampere-level nitrate electroreduction coupled with biomass upgrading. *Nat. Commun.* **2025**, *16*, 2392.

[10] Ma, Y. X.; Guo, X. Y.; Yuan, W. F.; Yang, P. N.; Zhang, Y.; Chen, W. X.; Cai, L. J.; Nicolosi, V.; Wang, W. L.; Chai, Y. et al. Paired electrochemical synthesis of glycolic acid and ammonia from polyester and nitrate sewage. *Chem Catal.* **2025**, *5*, 101336.

[11] Liang, J.; Li, Z. X.; Zhang, L. C.; He, X.; Luo, Y. S.; Zheng, D. D.; Wang, Y.; Li, T. S.; Yan, H.; Ying, B. W. et al. Advances in ammonia electrosynthesis from ambient nitrate/nitrite reduction. *Chem* **2023**, *9*, 1768–1827.

[12] Vitse, F.; Cooper, M.; Botte, G. G. On the use of ammonia electrolysis for hydrogen production. *J. Power Sources* **2005**, *142*, 18–26.

[13] Xi, W. L.; Yang, P.; Jiang, M. K.; Wang, X. L.; Zhou, H. X.; Duan, J. Y.; Ratova, M.; Wu, D. Electrochemical CO_2 reduction coupled with alternative oxidation reactions: Electrocatalysts, electrolytes, and electrolyzers. *Appl. Catal. B: Environ.* **2024**, *341*, 123291.

[14] Fan, L.; Jiang, R.; Da, Y. M.; Xiao, Y. K.; Jin, H. Q.; Chen, X.; Chen, W. Electrochemical ammonia oxidation reaction: From mechanistic understanding to practical applications. *InfoScience* **2024**, *1*, e12025.

[15] Zhang, Y. Z.; Chen, X.; Wang, W. L.; Yin, L. F.; Crittenden, J. C. Electrocatalytic nitrate reduction to ammonia on defective Au_1Cu (111) single-atom alloys. *Appl. Catal. B: Environ.* **2022**, *310*, 121346.

[16] Zhang, K. E.; Liu, Y.; Pan, Z. F.; Xia, Q.; Huo, X. Y.; Esan, O. C.; Zhang, X.; An, L. Cu-based catalysts for electrocatalytic nitrate reduction to ammonia: Fundamentals and recent advances. *EES Catal.* **2024**, *2*, 727–752.

[17] Luo, W. J.; Guo, Z. Y.; Ye, L.; Wu, S. L.; Jiang, Y. Y.; Xu, P.; Wang, H.; Qian, J. J.; Zhou, X. M.; Tang, H. et al. Electrical-driven directed-evolution of copper nanowires catalysts for efficient nitrate reduction to ammonia. *Small* **2024**, *20*, 2311336.

[18] Shih, Y. J.; Huang, Y. H.; Huang, C. P. Electrocatalytic ammonia oxidation over a nickel foam electrode: Role of $Ni(OH)_{2(s)}$-$NiOOH_{(s)}$ nanocatalysts. *Electrochim. Acta* **2018**, *263*, 261–271.

[19] Xu, W.; Lan, R.; Du, D. W.; Humphreys, J.; Walker, M.; Wu, Z. C.; Wang, H. T.; Tao, S. W. Directly growing hierarchical nickel-copper hydroxide nanowires on carbon fibre cloth for efficient electrooxidation of ammonia. *Appl. Catal. B: Environ.* **2017**, *218*, 470–479.

[20] Wang, Y. H.; Xu, A. N.; Wang, Z. Y.; Huang, L. S.; Li, J.; Li, F. W.; Wicks, J.; Luo, M. C.; Nam, D. H.; Tan, C. S. et al. Enhanced nitrate-to-ammonia activity on copper-nickel alloys via tuning of intermediate adsorption. *J. Am. Chem. Soc.* **2020**, *142*, 5702–5708.

[21] Biesinger, M. C.; Lau, L. W. M.; Gerson, A. R.; Smart, R. S. C. The role of the Auger parameter in XPS studies of nickel metal, halides and oxides. *Phys. Chem. Chem. Phys.* **2012**, *14*, 2434–2442.

[22] Biesinger, M. C. Advanced analysis of copper X-ray photoelectron spectra. *Surf. Interface Anal.* **2017**, *49*, 1325–1334.

[23] Pérez-Gallent, E.; Figueiredo, M. C.; Katsounaros, I.; Koper, M. T. M. Electrocatalytic reduction of Nitrate on Copper single crystals in acidic and alkaline solutions. *Electrochim. Acta* **2017**, *227*, 77–84.

[24] Zhang, S. B.; Li, K.; Zhang, X. Y.; Ye, Y. X.; Shi, T. F.; Jiang, Y.; Zheng, L. R.; Lin, Y.; Zhang, H. M. Concurrently selective electrosynthesis of ammonia and glycolic acid over cathodic single-atom cobalt and anodic PdNi alloying catalysts. *Adv. Funct. Mater.* **2025**, *35*, 2415046.

[25] Yu, W. Q.; Yu, J. Y.; Wang, Y. J.; Li, X.; Wang, Y. J.; Yuan, H. F.; Zhang, X. L.; Liu, H.; Zhou, W. J. Electrocatalytic upcycling of nitrate and hydrogen sulfide via a nitrogen-doped carbon nanotubes encapsulated iron carbide electrode. *Appl. Catal. B: Environ.* **2022**, *310*, 121291.

[26] Li, S. L.; Ma, P. J.; Gao, C. L.; Liu, L. J.; Wang, X. L.; Shakouri, M.; Chernikov, R.; Wang, K. W.; Liu, D. M.; Ma, R. G. et al. Reconstruction-induced NiCu-based catalysts towards paired electrochemical refining. *Energy Environ. Sci.* **2022**, *15*, 3004–3014.

[27] Daiyan, R.; Tran-Phu, T.; Kumar, P.; Iputera, K.; Tong, Z. Z.; Leverett, J.; Khan, M. H. A.; Asghar Esmailpour, A.; Jalili, A.; Lim, M. et al. Nitrate reduction to ammonium: From CuO defect engineering to waste NO_x-to-NH_3 economic feasibility. *Energy Environ. Sci.* **2021**, *14*, 3588–3598.

[28] Ye, S. H.; Chen, Z. D.; Zhang, G. K.; Chen, W. D.; Peng, C.; Yang, X.

Y.; Zheng, L. R.; Li, Y. L.; Ren, X. Z.; Cao, H. Q. et al. Elucidating the activity, mechanism and application of selective electrosynthesis of ammonia from nitrate on cobalt phosphide. *Energy Environ. Sci.* **2022**, *15*, 760–770.

[29] Wu, A. J.; Lv, J. B.; Xuan, X. X.; Zhang, J. H.; Cao, A.; Wang, M. J.; Wu, X. Y.; Liu, Q.; Zhong, Y. H.; Sun, W. et al. Electrocatalytic disproportionation of nitric oxide toward efficient nitrogen fixation. *Adv. Energy Mater.* **2023**, *13*, 2204231.

[30] Ye, J. Y.; Lin, J. L.; Zhou, Z. Y.; Hong, Y. H.; Sheng, T.; Rauf, M.; Sun, S. G. Ammonia electrooxidation on dendritic Pt nanostructures in alkaline solutions investigated by *in-situ* FTIR spectroscopy and online electrochemical mass spectroscopy. *J. Electroanal. Chem.* **2018**, *819*, 495–501.

[31] K, N. A.; Alzate-Carvajal, N.; Nallayagari, A. R.; Monyoncho, E. A.; Zulevi, B.; Serov, A.; Baranova, E. A. *In-situ* polarization modulation IRRAS investigation of ammonia electrooxidation on Pt–Ir and Pt–Ru nanoparticles prepared on engineered catalyst supports. *Electrochim. Acta* **2024**, *507*, 145046.

[32] Matsui, T.; Suzuki, S.; Katayama, Y.; Yamauchi, K.; Okanishi, T.; Muroyama, H.; Eguchi, K. *In situ* attenuated total reflection infrared spectroscopy on electrochemical ammonia oxidation over Pt electrode in alkaline aqueous solutions. *Langmuir* **2015**, *31*, 11717–11723.

[33] Yesudoss, D. K.; Ngozichukwu, B.; Gning, I.; Ngom, B. D.; Djire, A. Time-resolved fourier transform infrared spectroelectrochemical investigation of nitrate reduction to ammonia. *ACS Energy Lett.* **2025**, *10*, 1688–1699.

[34] Wang, Y. T.; Wang, C. H.; Li, M. Y.; Yu, Y. F.; Zhang, B. Nitrate electroreduction: Mechanism insight, *in situ* characterization, performance evaluation, and challenges. *Chem. Soc. Rev.* **2021**, *50*, 6720–6733.

[35] Janssens, T. V. W.; Falsig, H.; Lundegaard, L. F.; Vennestrøm, P. N. R.; Rasmussen, S. B.; Moses, P. G.; Giordanino, F.; Borfecchia, E.; Lomachenko, K. A.; Lamberti, C. et al. A consistent reaction scheme for the selective catalytic reduction of nitrogen oxides with ammonia. *ACS Catal.* **2015**, *5*, 2832–2845.

[36] Chen, R.; Yang, C. J.; Zhou, Z. F.; Haeffner, F.; Dersjant, A.; Dulock, N.; Dong, Q.; He, D.; Jin, J.; Zhao, Y. Y. et al. Electrochemically triggered chain reactions for the conversion of furan derivatives. *Angew. Chem., Int. Ed.* **2021**, *60*, 7534–7539.